

Synthesis and characterization of high surface area
 CuWO_4 and Bi_2WO_6 electrodes for use as photoanodes
for solar water oxidation†Cite this: *J. Mater. Chem. A*, 2013, **1**,
5006James C. Hill^a and Kyoung-Shin Choi^{*b}

Two n-type W-containing ternary oxides, CuWO_4 and Bi_2WO_6 , were prepared as high surface area electrodes and characterized for use as photoanodes in a water-splitting photoelectrochemical cell. The synthesis involved electrochemical preparation of porous WO_3 electrodes and annealing them with Cu^{2+} - or Bi^{3+} -containing solutions on their surfaces to form the respective electrodes. The resulting CuWO_4 electrode had a bandgap of 2.3 eV, and showed excellent photostability and photocurrent-to- O_2 conversion efficiency (ca. 100%) in 0.1 M borate buffer solution (pH 9). Bi_2WO_6 had a bandgap of 2.8 eV but, regardless of its higher bandgap energy, Bi_2WO_6 showed an earlier photocurrent onset and much higher photocurrent than CuWO_4 due to its more favorable CB edge and flatband potential position for water splitting. Bi_2WO_6 also showed chemical stability over a wide pH range ($-0.26 \leq \text{pH} \leq 9.0$). The photocurrent-to- O_2 conversion efficiency of Bi_2WO_6 was in the range of 50–75% and its photocurrent decayed over time, indicating photocorrosion. However, stable photocurrent was obtained when H_2O_2 , which has faster oxidation kinetics than water, was introduced into the electrolyte as a hole scavenger. This suggests that the photocorrosion of Bi_2WO_6 can be suppressed when an oxygen evolution catalyst is placed on its surface to improve interfacial hole transfer kinetics. With proper oxygen evolution catalysts and improved charge transport properties, both CuWO_4 and Bi_2WO_6 have the possibility of achieving better photoelectrochemical performances than WO_3 .

Received 16th January 2013
Accepted 28th February 2013

DOI: 10.1039/c3ta10245a

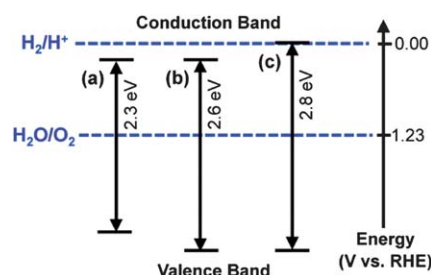
www.rsc.org/MaterialsA

Introduction

Tungsten oxide (WO_3), which is an n-type semiconductor, has been studied extensively as a photoanode for use in a water splitting photoelectrochemical cell because it is non-toxic, inexpensive, and chemically stable in acidic aqueous media.^{1–7} However, its bandgap energy allows for the utilization of only a limited portion of visible light ($E_g = 2.6\text{--}2.7$ eV). In addition, its conduction band (CB) edge, which is located at approximately 0.3 V vs. RHE, is not properly positioned for the photo-reduction of water to hydrogen. Furthermore, it often suffers from photo-instability due to incomplete water oxidation, generating and accumulating peroxy-species on its surface.^{3,5} Therefore, identifying new W-based oxide photoanodes that can address one or more of these issues while retaining the main advantages of WO_3 would be highly beneficial.

The most promising W-based ternary oxides for use as a photoanode for solar water oxidation include n-type CuWO_4 and n-type Bi_2WO_6 . CuWO_4 has a bandgap of 2.3–2.4 eV and

therefore can utilize significantly more visible light than WO_3 (Scheme 1).^{8,9} The reduction in bandgap is due to the valence band (VB) edge of CuWO_4 being more negative than that of WO_3 while the locations of CB edges are comparable in these two compounds. This is favorable because the VB edge of WO_3 allows photo-generated holes to have more than sufficient overpotential for water oxidation. Photoelectrochemical properties of CuWO_4 electrodes have been tested as a single component electrode and as a composite electrode (e.g. with p-type CuO and n-type WO_3).^{10–18} However, the characterization and the understanding of the photoelectrochemical properties of CuWO_4 photoanodes, specifically for use in solar water

Scheme 1 Schematic band diagrams of (a) CuWO_4 , (b) WO_3 , and (c) Bi_2WO_6 .^aDepartment of Chemistry, Purdue University, West Lafayette, IN 47907, USA^bDepartment of Chemistry, University of Wisconsin-Madison, Madison, WI 53706, USA. E-mail: kschoi@chem.wisc.edu; Fax: +1 608-262-0453; Tel: +1 608-262-5859

† Electronic supplementary information (ESI) available. See DOI: 10.1039/c3ta10245a

oxidation, have been limited with only a handful of papers published in this area. In particular, the chemical and photoelectrochemical stabilities of CuWO_4 have not been examined thoroughly as most of the previous studies did not show a current density–time plot under a constant bias condition, which is critical to assess its photo-stability as well as the photocurrent density independent of the potential scan rate.

Bi_2WO_6 is another ternary compound that has been shown to have potential use as a photoanode for solar water oxidation. Its band gap is reported to be 2.7–2.8 eV, which is slightly larger than the bandgap of WO_3 .^{19–26} As shown in Scheme 1a and c, the bandgap increase of Bi_2WO_6 is mainly due to the move of the CB edge to the negative direction and, therefore, it has the possibility of meeting the thermodynamic requirements to photoelectrochemically split water with little or no applied bias.^{27–30} The thermodynamic feasibility of photo-excited electrons in Bi_2WO_6 to reduce water to H_2 was demonstrated by Kudo and Hiji using powder-type Bi_2WO_6 photocatalysts with Pt deposited on the surface as a hydrogen evolution catalyst.²³ However, Bi_2WO_6 has been primarily studied as a powder-type photocatalyst for the photodegradation of organic pollutants to date,^{19–26} and studies on the synthesis and characterization of Bi_2WO_6 as an electrode-type photoanode for use in a water-splitting photoelectrochemical cell have been almost nonexistent. Only one study on electrode-type Bi_2WO_6 has been reported, where porous WO_3 prepared by the anodization of W metal was treated hydrothermally with bismuth nitrate to form Bi_2WO_6 electrodes.²⁵ In this study, photocurrent of Bi_2WO_6 was generated using a two-electrode system where a bias was applied between a Bi_2WO_6 photoanode and a Pt counter electrode. While the two-electrode system is critical for calculating the efficiency of the cell, it has limitations in precisely evaluating characteristics (*e.g.*, flatband potential, photocurrent onset, photocurrent density achievable at a constant potential) of the Bi_2WO_6 electrode, as no reference potential is available. In addition, the counter electrode performance as well as the working electrode performance affects the photocurrent generation in a two-electrode set up.

In this study, we report new synthesis procedures to prepare CuWO_4 and Bi_2WO_6 as high surface area porous electrodes by applying a simple chemical and heat treatment on high surface area porous WO_3 electrodes prepared by electrodeposition. In addition, we report the photoelectrochemical properties and stabilities of the resulting CuWO_4 and Bi_2WO_6 electrodes in various pH conditions to assess their promise for use as photoanodes for a water-splitting photoelectrochemical cell. By evaluating favorable and unfavorable features of these compounds, directions for future studies on W-based ternary oxides are provided.

Experimental section

Electrodeposition of porous WO_3 film

Both CuWO_4 and Bi_2WO_6 were prepared from electrochemically deposited porous WO_3 electrodes using a simple chemical and heat treatment. Detailed synthesis procedures and mechanisms for the cathodic electrodeposition of porous WO_3 electrodes can

be found elsewhere,⁴ but a brief description of the electrochemical synthesis is provided here. A 0.1 M tungsten (99.95%, <1 micron, Alfa Aesar) plating solution was prepared by oxidizing the tungsten metal to peroxo-tungstate with H_2O_2 (30%, Mallinckrodt) and decomposing the excess H_2O_2 with Pt black (Alfa Aesar). The plating solution was diluted to the appropriate concentration with deionized (DI) water and had a final composition of 50 v% ethylene glycol (Mallinckrodt). DI water used in this study was high-purity water obtained from a Millipore Milli-Q purified system (resistivity $\geq 18 \text{ M}\Omega$). The films were deposited in a 45 °C solution at -0.6 V (*vs.* Ag/AgCl) until 0.72 C of charge was passed (average current density = -1.4 mA cm^{-2}).⁴ The electrochemical setup consisted of fluorine doped tin oxide (FTO) coated glass (8–12 Ω resistance) as the working electrode, an Ag/AgCl (4 M KCl) reference electrode, and a glass slide sputter coated with 1000 Å of platinum on 300 Å of titanium as the counter electrode. A VMP2 multi-channel potentiostat (Princeton Applied Research) was used for all electrodepositions and photoelectrochemical measurements.

Synthesis of CuWO_4

100 μL of 0.2 M $\text{Cu}(\text{NO}_3)_2 \cdot 3\text{H}_2\text{O}$ (Acros, 99%) solution was pipetted onto the as-deposited WO_3 films (1 cm \times 2 cm \times 6 μm) to fully cover the surface of the film. The films were subsequently heated at 550 °C for 6 hours in air with a 2.2 °C min^{-1} ramping rate. During the heating procedure, WO_3 reacted with CuO to form CuWO_4 . Excess CuO that formed on the surface of the films during calcination was dissolved by soaking in a 0.5 M HCl bath for approximately 30 minutes to leave a pure CuWO_4 electrode. CuWO_4 is also slightly soluble in 0.5 M HCl but is less soluble than CuO . Therefore, the removal of CuO is possible by appropriately adjusting the soaking time.

Synthesis of Bi_2WO_6

100 μL of 0.2 M $\text{Bi}(\text{NO}_3)_3 \cdot 5\text{H}_2\text{O}$ (Sigma Aldrich, 98%) solution was pipetted onto the as-deposited WO_3 films (1 cm \times 2 cm \times 6 μm) to fully cover the surface of the film. Then the films were heated at 550 °C for 6 hours in air with a 2.2 °C min^{-1} ramping rate. During the heating procedure, WO_3 reacted with Bi_2O_3 to form Bi_2WO_6 . Excess Bi_2O_3 that formed at the surface of the Bi_2WO_6 electrode was dissolved by soaking in a 0.5 M HNO_3 solution at 40 °C for about 15 hours to leave a pure Bi_2WO_6 electrode.

Characterization

Powder X-ray diffraction (XRD) data was collected using a Scintag X2 or Bruker D8 diffractometer (Cu $\text{K}\alpha$ radiation). Absorbance was measured with a Cary 5000 UV-visible light spectrophotometer. Scanning electron microscopy (SEM) images and energy dispersive spectroscopy (EDS) data were acquired *via* a field emission scanning electron microscope (FEI Nova NanoSEM). The samples were first coated with *ca.* 2 nm thick Pt by a thermal evaporator to reduce charging and imaged at an accelerating voltage of 5 kV. The ratios obtained from EDS were collected at an accelerating voltage of 20 kV and analyzed using an Oxford Inca system coupled to the FEI Nova NanoSEM.

Capacitance measurements for Mott–Schottky plots were obtained using an EG&G Princeton Applied Research potentiostat (model 263A) linked with a Princeton Applied Research (FRD100) frequency response detector. A sinusoidal modulation of 10 mV was applied at frequencies of 5–20 kHz.

Photocurrent measurements

Photocurrent measurements were obtained with simulated solar illumination using a 300 W xenon arc lamp (Oriel) with intensity adjusted to 100 mW cm^{-2} by passing the beam through neutral density filters, an AM 1.5G filter, and a water filter. The beam passed through an optical fiber and illuminated 0.2 cm^2 of the sample through the FTO substrate (back-side illumination). For both CuWO_4 and Bi_2WO_6 electrodes, the back-side illumination generated much higher photocurrent than front-side illumination (*i.e.*, approximately a five-fold and a three-fold enhancement for CuWO_4 and Bi_2WO_6 , respectively), suggesting that the poor charge transport of electrons is one of the main limiting factors for photocurrent generation of these films.³¹ A fused silica cell was used and the setup consisted of CuWO_4 or Bi_2WO_6 films as the working electrode, or photoanode, a glass slide sputter coated with 1000 Å of platinum on 300 Å of titanium as the counter electrode, and an Ag/AgCl reference electrode (4 M KCl). Various electrolytes were used for photocurrent measurements, which

noise ratio because O_2 generated from the illuminated area of the sample was not substantial when standard illumination (100 mW cm^{-2} , AM 1.5G) was used. A custom-built airtight split cell divided with a frit, 13 mm O.D. was used for all O_2 measurements. The split cell was made airtight by plastic caps with *o*-rings and copper rods inserted through the cap to attach the electrodes *via* copper adhesive tape. The oxygen sensor consisted of a platinum–porphyrin-based fluorescence sensor, FOSPOR-R 1/16" (Ocean Optics), inserted into the septum on the cap of the split cell. A two point calibration was performed using argon as 0% O_2 and air as 20.9% O_2 . Both sides of the split cell were filled with 30 mL of electrolyte and had approximately 15 mL of headspace. The solution and headspace were purged with argon. The split cell was not completely airtight and slowly leaked air into the compartment. Therefore a leak rate was calculated and subtracted from the experimental data by determining the slope of the baseline before and after photoelectrochemical measurements were taken. The probe measured actual O_2 produced in mole percent, which was converted to micromoles of O_2 after accounting for O_2 dissolved in the electrolyte with Henry's Law. The theoretical amount of O_2 produced was determined by assuming the amount of charge passed during illumination corresponded to 100% Faradaic efficiency toward O_2 evolution. Thus the photocurrent-to- O_2 conversion efficiency was measured by the following equation (eqn (1))

$$\text{photocurrent to } \text{O}_2 \text{ conversion efficiency (\%)} = \frac{\text{actual amount of } \text{O}_2 \text{ detected}}{\text{expected amount of } \text{O}_2 \text{ produced based on photocurrent}} \times 100\%$$

include 1–0.05 M H_2SO_4 , 1 M NaOH, 0.1 M phosphate buffer (pH 7), and 0.1 M borate buffer (pH 9). The phosphate buffer was prepared by dissolving 0.1 M NaH_2PO_4 in DI water and adjusting the pH to 7 with NaOH. The borate buffer was prepared by dissolving 0.1 M H_3BO_3 in DI water and adjusting the pH to 9 with NaOH. For some cases, H_2O_2 (0.5 M) was added as a hole acceptor. Photocurrent density (J)–potential (V) plots were obtained using a potential scan rate of 10 mV s^{-1} . While all measurements were carried out using an Ag/AgCl (4 M KCl) reference electrode, results in this study were presented against the reversible hydrogen electrode (RHE) for ease of comparison with the H_2 and O_2 redox levels and with other literature reports that used electrolytes with different pH conditions by converting the potential using the following equation.

$$E \text{ (vs. RHE)} = E \text{ (vs. Ag/AgCl)} + E_{\text{Ag/AgCl}} \text{ (ref)} + 0.0591 \text{ V} \times \text{pH}$$

$$(E_{\text{Ag/AgCl}} \text{ (ref)} = 0.1976 \text{ V vs. NHE at } 25^\circ\text{C})$$

Oxygen detection

Oxygen measurements were performed using 400 mW cm^{-2} illumination with an AM 1.5G filter to ensure a higher signal-to-

Results and discussion

CuWO_4

Porous CuWO_4 electrodes were prepared by applying a simple chemical and thermal treatment to porous WO_3 electrodes prepared by electrodeposition. Electrodeposition of porous WO_3 electrodes was carried out cathodically by applying -0.6 V vs. Ag/AgCl to the FTO working electrode immersed in a 0.1 M polyperoxo-tungstic acid solution containing 50 v% ethylene glycol at 45°C . The use of ethylene glycol and an elevated deposition temperature were critical in obtaining porous morphologies. Detailed deposition conditions and mechanisms can be found elsewhere.⁴ The as-deposited film was amorphous, which is most likely composed of a hydrated form of WO_3 . This film could be converted to a crystalline WO_3 film by annealing at 500°C for 1 hour in the air. The SEM images depicted in Fig. 1a and b show the porous nature of the as-deposited and annealed WO_3 electrodes.

In order to prepare CuWO_4 electrodes, 100 μL of 0.2 M $\text{Cu}(\text{NO}_3)_2 \cdot 3\text{H}_2\text{O}$ solution was pipetted onto the as-deposited WO_3 films ($1 \text{ cm} \times 2 \text{ cm} \times 6 \mu\text{m}$) to fully cover its surface. The films were then heated at 350 – 550°C for 6 hours in air. During the heating procedure, the Cu^{2+} ions formed CuO layers surrounding each WO_3 particle enabling the solid state reaction to occur between the CuO and WO_3 to form CuWO_4 . Since the

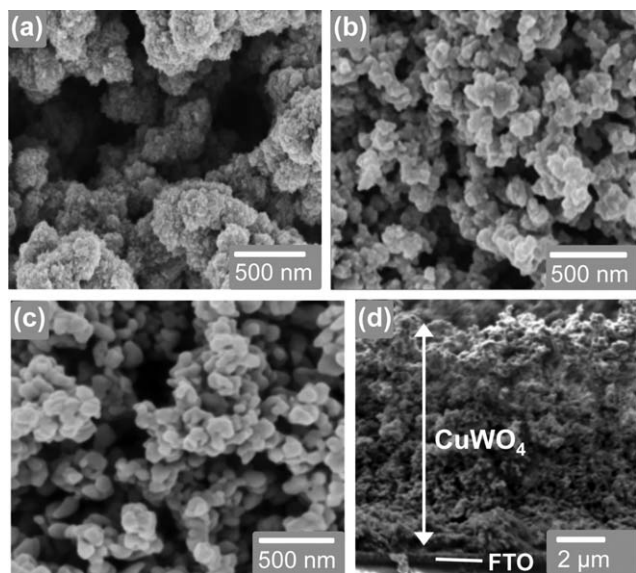


Fig. 1 Top-view SEM images of (a) as-deposited amorphous WO_3 , (b) crystalline WO_3 , and (c) CuWO_4 electrodes. (d) Side-view SEM image of a CuWO_4 electrode is also shown.

Cu^{2+} -solution contained more Cu^{2+} ions than were necessary to fully convert WO_3 to CuWO_4 , CuO residues remained on the CuWO_4 surface after annealing. The excess CuO was removed by soaking the electrode in a 0.5 M HCl solution to leave a pure CuWO_4 electrode. An SEM image of the resulting CuWO_4 electrode, which was obtained by annealing at 550 °C, is shown in Fig. 1c where nano-size CuWO_4 particles are interconnected, retaining the original porosity (Fig. 1c and d). The schematic representation of the synthesis procedure is summarized in Scheme 2.

Fig. 2 shows XRD patterns of the electrodes obtained after annealing the amorphous WO_3 electrodes with Cu^{2+} -containing solution at three different temperatures (350 °C, 450 °C, and 550 °C) for 6 hours, followed by the removal of excess CuO . (The XRD pattern before the removal of CuO is shown in ESI, Fig. S1.†) The films annealed at 350 °C were still amorphous while the film annealed at 450 °C showed peaks from both crystalline WO_3 (JCPDF: 43-1035) and CuWO_4 phases (JCPDF: 73-1823). The film annealed at 550 °C showed only CuWO_4

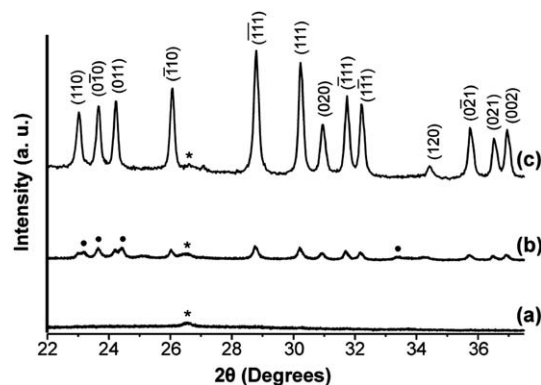
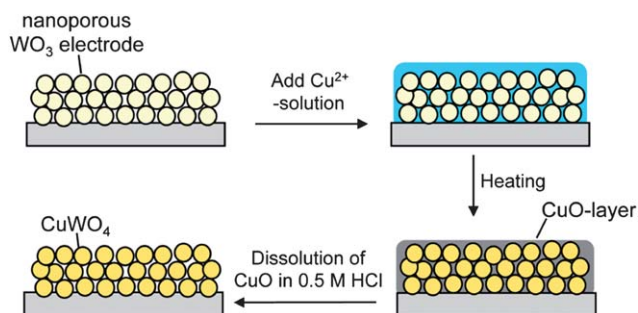


Fig. 2 XRD patterns of Cu^{2+} -containing WO_3 electrodes annealed at (a) 350 °C, (b) 450 °C, and (c) 550 °C for 6 hours followed by the removal of CuO in acid. Peaks from the FTO substrate and WO_3 are denoted by * and •, respectively.

peaks, indicating that the complete conversion of WO_3 and CuO to CuWO_4 can be achieved at this temperature. The use of higher annealing temperatures and/or longer annealing times yielded CuWO_4 electrodes that generate lower photocurrent, most likely due to extensive particle agglomeration, reducing the surface area. To further verify the purity of the CuWO_4 electrode and the absence of any amorphous impurity phases, the sample obtained by annealing at 550 °C was analyzed by EDS and a chemical formula of $\text{CuW}_{1.05}\text{O}_{4.09}$ was obtained.

It should be noted that preparing CuWO_4 by solid state reactions of WO_3 and CuO powders would require heating the mixture to at least 800 °C for complete conversion.¹² The reason why the conversion was achieved at a much lower temperature in this study is partly because the individual grain size of WO_3 was very small (*ca.* 100–300 nm in diameter) and Cu^{2+} was provided as a solution phase, which allowed for easy penetration of Cu^{2+} ions into the porous WO_3 film, which upon annealing form intimate WO_3/CuO contacts. However, a more critical factor was the thermal instability of the amorphous hydrated WO_3 phase, which is converted to a crystalline WO_3 phase at around 450 °C. It appears that the conversion of the hydrated amorphous WO_3 phase to a crystalline phase promotes the formation of CuWO_4 at a much lower temperature. As evidence, if the same Cu^{2+} and heat treatments were performed on crystalline WO_3 electrodes having the same porosity, complete conversion to CuWO_4 could not be achieved at 550 °C.

The UV-vis absorbance spectrum of the CuWO_4 electrode is shown in Fig. 3a in comparison with that of the crystalline WO_3 electrode having the same morphology. From these spectra, the bandgaps of CuWO_4 and WO_3 were estimated to be *ca.* 2.3 eV and *ca.* 2.7 eV, respectively. The photoelectrochemical properties and stabilities of CuWO_4 were investigated in several electrolytes including 0.5 M H_2SO_4 , 0.05 M H_2SO_4 , 1 M NaOH , 0.1 M sodium phosphate buffer (pH 7), and 0.1 M borate buffer (pH 9). However, CuWO_4 was chemically not stable in 0.5 M H_2SO_4 or 1 M NaOH solutions. Therefore, only the photocurrent density–potential characteristics (*J*–*V* plot) obtained in 0.05 M H_2SO_4 (pH 1), 0.1 M sodium phosphate buffer (pH 7) and 0.1 M borate



Scheme 2 Schematic representation for the conversion of a nanoporous amorphous WO_3 electrode to a CuWO_4 electrode.

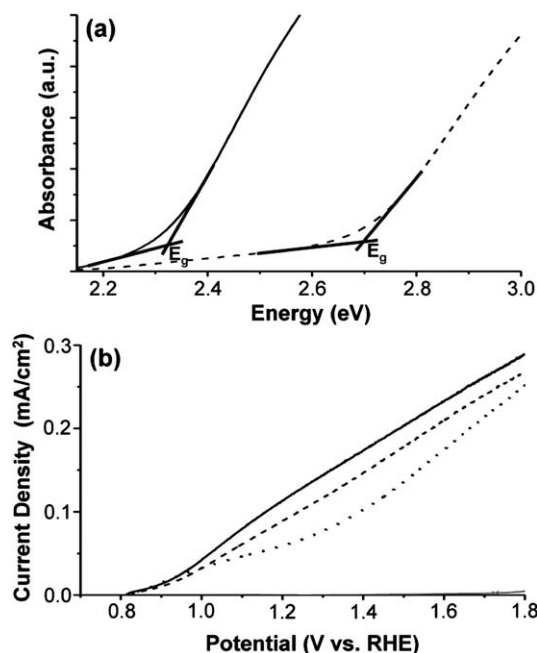


Fig. 3 (a) UV-vis absorption spectra of crystalline WO_3 (dashed) and CuWO_4 (solid) electrodes. (b) J - V plots of CuWO_4 measured in 0.1 M borate buffer (pH 9) (solid), 0.1 M phosphate buffer (pH 7) (dashed), and 0.05 M H_2SO_4 solution (pH 1) (dotted) under AM 1.5G, 100 mW cm^{-2} illumination (scan rate = 10 mV s^{-1}). Dark current is shown as a gray line.

buffer (pH 9) are shown in Fig. 3b. (For comparison, WO_3 is chemically stable in strong acidic solutions but not stable in neutral or basic solutions.) For easy comparison, the thermodynamic pH effect on the oxidation potential of water was removed by plotting the current against the potential vs. RHE. The results show that the performances of CuWO_4 in the phosphate (pH 7) and borate buffer (pH 9) solutions were comparable but the performance in the borate buffer was slightly better. The photocurrent of CuWO_4 obtained in 0.05 M H_2SO_4 (pH 1) was the lowest. Therefore, the remainder of the photoelectrochemical characterizations for CuWO_4 were performed in a 0.1 M borate buffer solution (pH 9).

Fig. 4a shows Mott-Schottky plots for CuWO_4 obtained in 0.1 M borate buffer (pH 9). The flat band potential was slightly frequency dependent, probably due to its nanoparticulate nature. Nevertheless, the average value, which is estimated to be approximately 0.42 V vs. RHE, agrees with the previously reported values.^{14,16} The significant difference between the flatband potential and the photocurrent onset potential determined by Fig. 3b, which is ca. 0.8 V vs. RHE, suggests that the photogenerated electron-hole pairs are not effectively separated in the low-bias region, delaying the photocurrent onset.

In order to confirm that the photocurrent generated by CuWO_4 is all associated with O_2 production, photocurrent measurement and O_2 detection were carried out simultaneously at 0.4 V vs. Ag/AgCl (1.13 V vs. RHE) under 400 mW cm^{-2} illumination with an AM 1.5G filter. The conditions for this experiment (intense light, high bias) were chosen to ensure sufficient generation of O_2 and, therefore, more reliable O_2

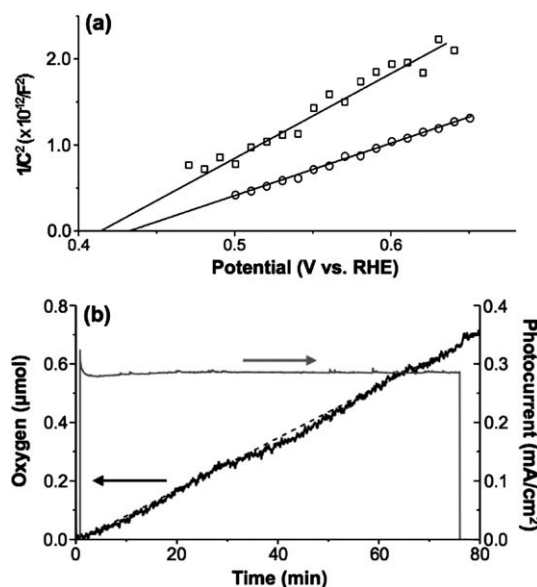


Fig. 4 (a) Mott-Schottky plots for a CuWO_4 electrode obtained in 0.1 M borate buffer (pH 9) at 15 kHz (O) and 20 kHz (□). (b) Oxygen measurement obtained at 0.4 V vs. Ag/AgCl (1.13 V vs. RHE) in 0.1 M borate buffer (pH 9) (400 mW cm^{-2} illumination with an AM 1.5G filter) comparing the actual amount of O_2 produced (solid) and the theoretical amount of O_2 (dashed) calculated assuming 100% Faradaic photocurrent-to- O_2 conversion efficiency. A photocurrent density-time profile for the O_2 measurement is shown as a gray line.

detection. Fig. 4b shows both the expected amount of O_2 calculated from the photocurrent generated, assuming 100% Faradaic conversion efficiency, and the actual amount of O_2 detected by the O_2 sensor. The results show that approximately 100% of the photocurrent contributed to the oxidation of water to form O_2 . In addition, very stable photocurrent density of 0.58 mA cm^{-2} was maintained during the O_2 measurement.

Recently, Bartlett and Yourey prepared CuWO_4 electrodes by co-electrodepositing copper oxides (CuO and Cu_2O) and tungsten oxide *via* potential cycling followed by thermal annealing to react copper oxides and tungsten oxide.¹⁴ Since the ratio of Cu to W in the as-deposited film was not exactly 1 : 1 with excess W, the annealing procedure generated $\text{CuWO}_4/\text{WO}_3$ composite electrodes. The resulting electrode showed promising performance, but the current density-time plot obtained in a pH 7 phosphate buffer at 0.5 V vs. Ag/AgCl (1.11 V vs. RHE) shows a gradual decrease in photocurrent over time. Since the composite electrode also contained WO_3 , which is known to consume a portion of holes for partial oxidation of water to hydrogen peroxide that makes the surface photo-inactive over-time,³⁻⁵ it was difficult to know whether the observed photo-instability is due to the CuWO_4 component or due to the WO_3 component. Our result shown in Fig. 4b confirms that CuWO_4 is stable in a borate buffer (pH 9). Also, a photocurrent-time plot of a CuWO_4 electrode obtained under AM 1.5G, 100 mW cm^{-2} illumination in a phosphate buffer (pH 7) looks stable (ESI, Fig. S2†), suggesting that the observed instability of the $\text{CuWO}_4/\text{WO}_3$ composite electrode is most likely due to the well-documented photocorrosion of the WO_3 component during the photooxidation of water.^{3,5} Our study demonstrates that the

photostability toward the water oxidation reaction and the *ca.* 100% photocurrent-to-O₂ conversion ratio of CuWO₄ are distinctive advantages of CuWO₄ over WO₃.

In order to ascertain whether the photocurrent of CuWO₄ was limited by the poor catalytic ability of the CuWO₄ surface for water oxidation, photocurrent was measured in the presence of 0.5 M H₂O₂ as a hole scavenger. The oxidation of H₂O₂ (eqn (2)) is known to be kinetically much faster than the oxidation of water (eqn (3)).^{32,33}

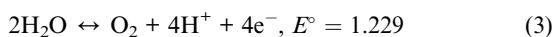
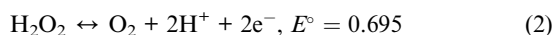


Fig. 5a shows the photocurrent comparison measured with and without H₂O₂ at 0.3 V *vs.* Ag/AgCl (1.03 V *vs.* RHE). The result shows that the addition of H₂O₂ increased the photocurrent approximately four-fold, suggesting that improving O₂ evolution kinetics by placing an appropriate O₂ catalyst would definitely improve the photocurrent of CuWO₄ for solar water oxidation. However, the *J*-*V* plot obtained in the presence of H₂O₂ shows that the photocurrent onset potential is shifted only slightly to the negative direction (from 0.9 V to 0.85 V) and it is still very distant from the flatband potential value determined by the Mott-Schottky plots (Fig. 5b). Also, the overall photocurrent is still much lower than what is expected based on its bandgap energy. This indicates that the major limitation of our CuWO₄ electrodes is its poor electron-hole separation efficiency, which could be improved by optimizing carrier densities and charge transport properties. Despite relatively low photocurrent observed in this study, the photostability and the excellent photocurrent-to-O₂ conversion ratio as well as its smaller bandgap suggest that CuWO₄ is a promising photoanode candidate, which requires further studies for optimization.

Bi₂WO₆

Porous Bi₂WO₆ electrodes were prepared from as-deposited porous WO₃ electrodes using the same method used for the

preparation of porous CuWO₄ electrodes, except for the type of solution used for chemical treatment. In this case, 1 M HNO₃ solution containing 0.2 M Bi(NO₃)₃ was used as the source of Bi³⁺. 100 μL of this solution was placed on the as-deposited WO₃ film to fully cover the surface, then annealed at 550 °C for 6 hours in air. After annealing, excess Bi₂O₃ was removed in a 0.5 M HNO₃ solution. (The XRD pattern before the removal of Bi₂O₃ is shown in ESI, Fig. S3.†)

The XRD pattern of the Bi₂WO₆ film obtained after annealing and removing Bi₂O₃ shows a set of peaks that belong to the Bi₂WO₆ phase (γ-Bi₂WO₆, JCPDF # 39-0256) (Fig. 6). An SEM image of the Bi₂WO₆ electrode is shown in Fig. 7a. Unlike the conversion from the amorphous WO₃ to CuWO₄, the original morphology was not retained and reduction of surface area was obvious, although it still has some porous features. The observed grain growth and reduction in surface area seems to be inevitable due to the significant volume and mass increase caused by incorporating two Bi atoms and three O atoms per one WO₃ formula unit to form Bi₂WO₆. For comparison, conversion of WO₃ to CuWO₄ requires an addition of only one Cu atom and one O atom per one WO₃ formula unit and, therefore, the mass/volume gain by this conversion is less significant, which is why the surface morphology and the surface area did not change considerably in this case (Fig. 1). The volume per formula unit of WO₃, CuWO₄, and Bi₂WO₆

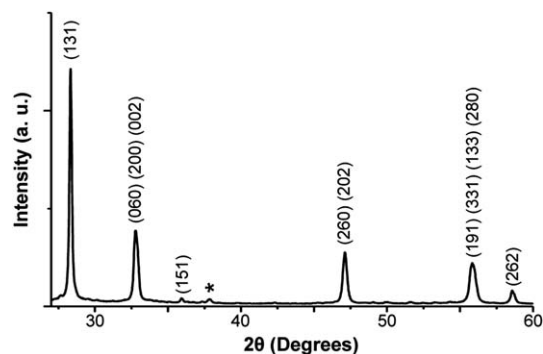


Fig. 6 XRD pattern of a Bi₂WO₆ electrode obtained after annealing and the removal process of Bi₂O₃. Peaks from the FTO substrate are denoted by *, respectively.

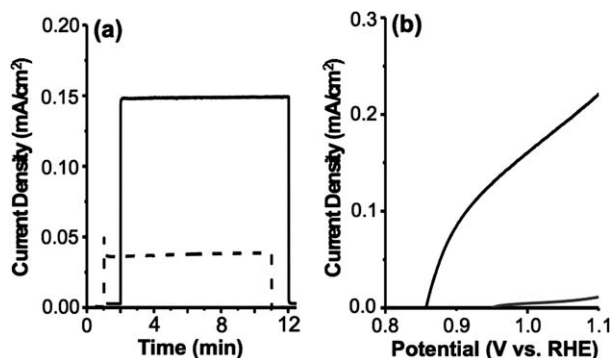


Fig. 5 (a) Photocurrent of a CuWO₄ photoanode obtained at 0.3 V *vs.* Ag/AgCl (1.03 V *vs.* RHE) in a 0.1 M borate buffer (pH 9) with (solid line) and without (dashed line) 0.5 M hydrogen peroxide under 100 mW cm⁻², AM 1.5G illumination. (b) *J*-*V* plot of a CuWO₄ electrode measured in 0.1 M borate buffer (pH 9) with 0.5 M H₂O₂ under AM 1.5G, 100 mW cm⁻² illumination (scan rate = 10 mV s⁻¹). Dark current is shown as gray line.

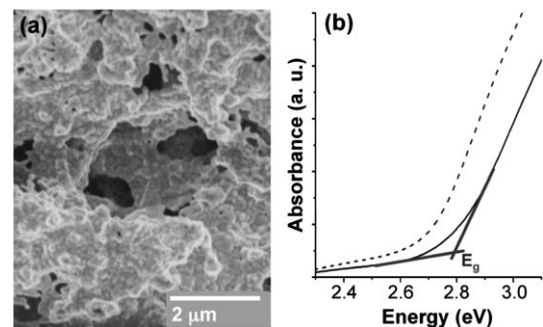


Fig. 7 (a) Top-view SEM image and (b) UV-vis spectrum of Bi₂WO₆ (solid line). UV-vis spectrum of WO₃ (dashed line) is also shown for comparison. (Side-view SEM image of Bi₂WO₆ is shown in ESI, Fig. S4.†)

calculated using the crystal structures stabilized in this study are 52.8 \AA^3 , 66.4 \AA^3 , and 121.9 \AA^3 , respectively.

The UV-vis absorption spectrum of a yellow-white Bi_2WO_6 electrode is shown in Fig. 7b, which confirms that the bandgap of Bi_2WO_6 (2.8 eV) is slightly larger than that of WO_3 (Fig. 7b).

The photoelectrochemical properties and stabilities of Bi_2WO_6 were investigated in 1 M and 0.05 M H_2SO_4 , 1 M NaOH, 0.1 M phosphate buffer (pH 7), 0.1 M borate buffer (pH 9), and 1 M NaOH solutions. Bi_2WO_6 was chemically stable in all solutions except 1 M NaOH. The photocurrent density–potential (J – V) plots obtained in the phosphate buffer (pH 7) and the borate buffer (pH 9) were almost identical and, therefore, only the photocurrent obtained in the borate buffer is shown in Fig. 8a. Bi_2WO_6 showed enhanced photocurrent in 0.05 M H_2SO_4 , but the performance decreased as the solution became more acidic (Fig. 8a). Therefore, further characterizations of Bi_2WO_6 were performed in a borate buffer (pH 9) and in a 0.05 M H_2SO_4 solution to compare its performances in acidic and slightly basic media.

The Mott–Schottky plots obtained in these two solutions are compared in Fig. 8b and c. The plots obtained in the borate buffer showed significant frequency-dependence, suggesting that the Mott–Schottky plot may not be used to accurately determine the flatband potential of the nanoporous Bi_2WO_6 electrode, possibly due to it having a poorly defined space-charge region and severe surface states. The flatband potentials

obtained at 5 kHz and 10 kHz were 0.17 V vs. RHE and -0.02 V vs. RHE, respectively. The value obtained at 10 kHz agrees well with the previous study reporting the thermodynamic feasibility of Bi_2WO_6 to produce H_2 . The x -intercepts of the Mott–Schottky plots obtained at 5 kHz (0.27 V vs. RHE) and 10 kHz (0.20 V vs. RHE) in 0.05 M H_2SO_4 also showed a frequency-dependence, although the variation is less significant. Also, the average x -intercept was different from that obtained in 0.1 M borate buffer. The pH dependence of the flatband potential, when reported against RHE to eliminate the effect of the pH-dependent Helmholtz layer potential drop, suggests that our high surface area Bi_2WO_6 electrode does not behave like an ideal oxide-based electrode that can achieve acid–base equilibrium in a solution at any pH value.^{34,35} Nonetheless, using the results obtained from the Mott–Schottky plots it could be assumed that the flatband potential of Bi_2WO_6 is at least *ca.* 200 mV more negative than that of CuWO_4 .

When comparing the photocurrent densities of CuWO_4 and Bi_2WO_6 for water oxidation, although the bandgap of Bi_2WO_6 is much wider than that of CuWO_4 , Bi_2WO_6 shows much higher photocurrent. For example, the potential necessary to achieve 0.1 mA cm^{-2} in 0.1 M borate buffer was 1.16 V vs. RHE and 0.95 V vs. RHE for CuWO_4 and Bi_2WO_6 , respectively. This is mainly due to the more negative flatband potential of Bi_2WO_6 , which results in earlier photocurrent onset. This clearly demonstrates the importance of the CB and flatband potential positions in evaluating photoanodes for use in solar water splitting. The assessment of photoanodes purely based on bandgap energy without considering their CB and VB edge positions will be meaningful only for comparing photon absorption-limited photocurrents that can be achieved in the high bias region. However, what is critical in achieving high efficiency in photoanodes and photoelectrochemical diodes is to achieve the maximum power point in the lower bias region.^{36,37} Therefore, although Bi_2WO_6 has a disadvantage in terms of bandgap energy, it is still possible that Bi_2WO_6 achieves a higher efficiency than CuWO_4 owing to its CB being *ca.* 400 mV more negative than that of CuWO_4 (Scheme 1).

The photocurrent–time plots obtained while applying a constant potential of 1.03 V vs. RHE in 0.1 M borate buffer and 0.05 M H_2SO_4 are shown in Fig. 9a and b (dashed lines). As expected from their J – V plots, the initial photocurrent obtained in the 0.05 M H_2SO_4 solution was much higher (*i.e.* more than 200% enhancement). However, in both solutions the photocurrent decayed gradually, indicating photocorrosion. Indeed, when O_2 produced by the Bi_2WO_6 photoanode is measured and compared with the theoretical amount of O_2 calculated from the photocurrent assuming 100% Faradaic efficiency, the photocurrent-to- O_2 conversion efficiency was estimated to be only about 50% and 72% in 0.1 M borate buffer and 0.05 M H_2SO_4 , respectively (Fig. 9c and d), indicating that the rest of the photocurrent is most likely used for photocorrosion.

However, when 0.5 M hydrogen peroxide was added to these solutions, not only the initial photocurrent density was increased (by 64% in 0.1 M borate buffer and by 9% in 0.05 M H_2SO_4), but also photocurrent decay disappeared (Fig. 9a and b, solid lines). This is a good indication that the poor water

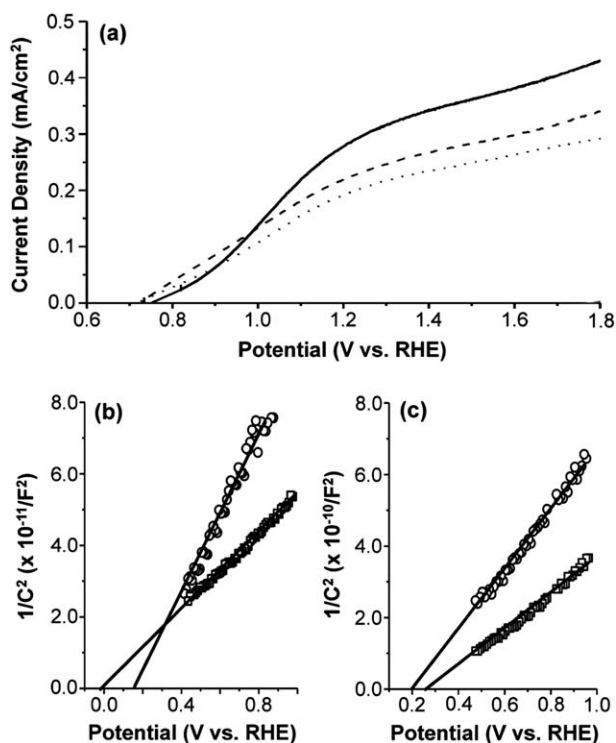


Fig. 8 (a) J – V plots of Bi_2WO_6 measured in 0.1 M borate buffer (pH 9) (dotted), in 0.05 M H_2SO_4 (pH 1) (solid), and in 1.0 M H_2SO_4 (pH -0.26) (dashed) under AM 1.5G, 100 mW cm^{-2} illumination (scan rate = 10 mV s^{-1}). Mott–Schottky plots of Bi_2WO_6 obtained (b) in 0.1 M borate buffer and (c) in 0.05 M H_2SO_4 at 5 kHz (\circ) and 10 kHz (\square).

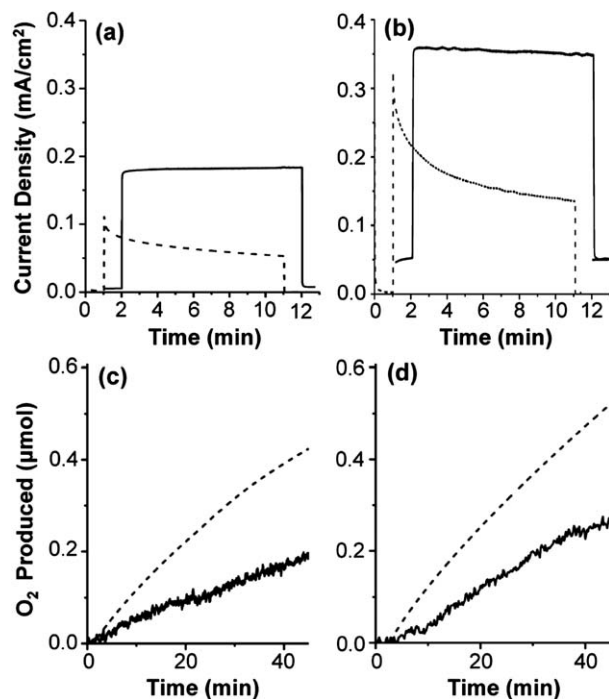


Fig. 9 Photocurrent of a Bi_2WO_6 photoanode obtained at 1.03 V vs. RHE in (a) 0.1 M borate buffer (pH 9) and (b) 0.05 M H_2SO_4 (pH 1) with (solid) and without (dashed) 0.5 M hydrogen peroxide under AM 1.5G, 100 mW cm^{-2} illumination. Oxygen measurements of a Bi_2WO_6 photoanode obtained at 1.13 V vs. RHE in (c) 0.1 M borate buffer (pH 9) and (d) 0.05 M H_2SO_4 (pH 1) (400 mW cm^{-2} illumination with an AM 1.5G filter) comparing the actual amount of O_2 produced (solid) and the theoretical amount of O_2 (dashed) calculated assuming 100% Faradaic photocurrent-to- O_2 conversion efficiency.

oxidation kinetics of the Bi_2WO_6 photoanode was mainly responsible for the low photocurrent and photocorrosion. Therefore, if the water oxidation kinetics is improved by adding OECs on the Bi_2WO_6 surface, the Bi_2WO_6 photoanode is expected to produce much higher and stable photocurrent for water oxidation.

The J - V plots of the Bi_2WO_6 photoanode for H_2O_2 oxidation in 0.1 M borate buffer (pH 9) and 0.05 M H_2SO_4 (pH 1) are shown in Fig. 10. It shows a significant photocurrent increase in the overall potential range compared to photocurrent for water oxidation shown in Fig. 8a. For example, the potential necessary to achieve 0.1 mA cm^{-2} in 0.1 M borate buffer was 0.99 V vs. RHE and 0.70 V vs. RHE for water oxidation and H_2O_2 oxidation, respectively. In 0.05 M H_2SO_4 , the potential necessary to achieve 0.1 mA cm^{-2} was 0.95 V vs. RHE and 0.64 V vs. RHE for water oxidation and H_2O_2 oxidation, respectively.

However, in both solutions, the shift of the photocurrent onset potential to the negative direction achieved by adding H_2O_2 was not considerable (by 0.04 V in 0.1 M borate buffer and by 0.16 V in 0.05 M H_2SO_4), and the photocurrent onset potentials were still very distant from their estimated flatband potential. Also, the overall photocurrent generation was not significant. This indicates that, like the CuWO_4 electrodes, the Bi_2WO_6 electrodes also suffer from a low electron-hole separation efficiency. Judging from the fact that the back-side

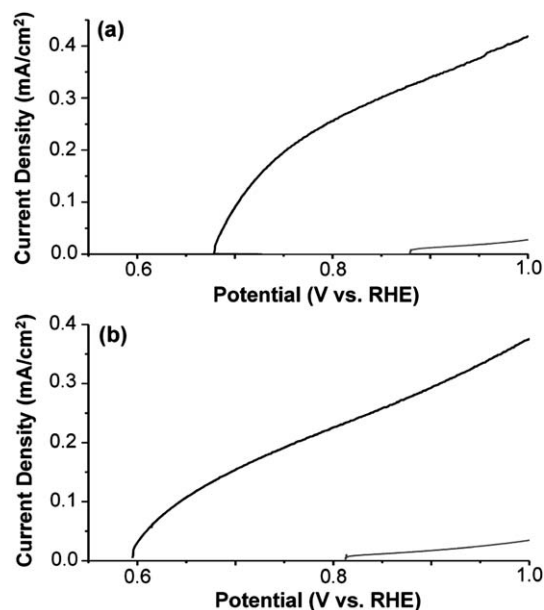


Fig. 10 J - V plots of a Bi_2WO_6 photoanode in (a) 0.1 M borate buffer (pH 9) and (b) 0.05 M H_2SO_4 , both containing 0.5 M hydrogen peroxide under AM 1.5G, 100 mW cm^{-2} illumination (scan rate = 10 mV s^{-1}). Dark currents are shown as gray lines.

illumination generated much higher photocurrent than the front-side illumination for both the CuWO_4 and Bi_2WO_6 electrodes (see the Experimental section), poor electrical conductivity is one of the limiting factors for photocurrent generation.³¹ Therefore, optimization of charge transport properties would be the most straightforward future study to lead to the performance enhancement of these photoelectrodes.

Conclusions

Two n-type W-based semiconductor electrodes, CuWO_4 and Bi_2WO_6 , which can be potentially used as photoanodes for a solar water splitting photoelectrochemical cell, have been prepared as high surface area polycrystalline electrodes. The synthesis procedure involved electrochemical preparation of amorphous high surface area WO_3 electrodes and coating them with a 200 mM solution of the corresponding metal nitrate salts. The thermal conversion of WO_3 to CuWO_4 and Bi_2WO_6 was achieved by heating the samples at 550°C and removing any residual CuO or Bi_2O_3 by dissolution in an acid solution, resulting in pure CuWO_4 and Bi_2WO_6 electrodes. Compared to WO_3 , CuWO_4 showed improved chemical stability in neutral and slightly basic solutions although it was not as stable as WO_3 in strong acidic media ($\text{pH} < 1$). Also, CuWO_4 showed no sign of photocorrosion and excellent photocurrent-to- O_2 conversion efficiency in 0.1 M borate buffer (pH 9). Bi_2WO_6 also showed much promise as a photoanode for solar water splitting. It generated higher photocurrent than CuWO_4 for water oxidation due to its more negative CB and flatband potential, although its bandgap is much higher (2.8 eV). Also, its chemical stability in solutions of a wide pH range ($-0.26 \leq \text{pH} \leq 9$) was a distinctive advantage. Its photocurrent-to- O_2 conversion efficiency was

limited to 50% and 72% in 0.1 M borate buffer and 0.05 M H_2SO_4 , respectively, and the photocurrent decayed gradually over time indicating photocorrosion. However, stable photocurrent was obtained when the interfacial hole transfer kinetics was improved by adding H_2O_2 into the electrolyte. This suggests that the photocorrosion of Bi_2WO_6 is not due to the intrinsic photo-instability of Bi_2WO_6 , but due to its poor water oxidation kinetics, which may be suppressed when an OEC layer is placed on the surface. With further efforts toward improving charge transport properties and adding suitable OEC layers, both CuWO_4 and Bi_2WO_6 have the possibility to exceed the performance of WO_3 as a photoanode for use in a photo-electrochemical cell for water splitting.

Acknowledgements

This work was supported by the Division of Chemical Sciences, Geosciences, and Biosciences, Office of Basic Energy Sciences of the U.S. Department of Energy through Grant DE-FG02-12ER16310 and made use of the Life Science Microscopy Facility at Purdue University.

References

- 1 C. Santato, M. Odziemkowski, M. Ulmann and J. Augustynski, *J. Am. Chem. Soc.*, 2001, **123**, 10639.
- 2 B. Yang, P. Barnes, W. Bertram and V. Luca, *J. Mater. Chem.*, 2007, **17**, 2722.
- 3 J. Augustynski, R. Solarska, H. Hagemann and C. Santato, *Proc. SPIE*, 2006, **6340**, U140–U148.
- 4 J. C. Hill and K.-S. Choi, *J. Phys. Chem. C*, 2012, **116**, 7612.
- 5 J. Seabold and K.-S. Choi, *Chem. Mater.*, 2011, **23**, 1105.
- 6 Q. Mi, A. Zhanaidarova, B. Brunschwig, H. Gray and N. Lewis, *Energy Environ. Sci.*, 2012, **5**, 5694.
- 7 L. Weinhardt, M. Blum, M. Bär, C. Heske, B. Cole, B. Marsen and E. Miller, *J. Phys. Chem. C*, 2008, **112**, 3078.
- 8 T. Montini, V. Gombac, H. Hameed, L. Felisari, G. Adami and P. Fornasiero, *Chem. Phys. Lett.*, 2010, **498**, 113.
- 9 M. Lalic, Z. Popovic and F. Vukajlovic, *Comput. Mater. Sci.*, 2011, **50**, 1179.
- 10 V. Atuchin, I. Troitskaia, O. Khyzhun, V. Bekenev and Y. Solonin, *Appl. Mech. Mater.*, 2012, **110–116**, 2188.
- 11 F. Benko, C. MacLaurin and F. Koffyberg, *Mater. Res. Bull.*, 1982, **17**, 133.
- 12 L. Dorfman, D. Houck, M. Scheithauer, J. Dann and H. Fassett, *J. Mater. Res.*, 2001, **16**, 1096.
- 13 R. Lacombe-Perales, J. Ruiz-Fuertes, D. Errandonea, D. Martinez-Garcia and A. Segura, *Europhys. Lett.*, 2008, **83**, 37002.
- 14 J. Yourey and B. Bartlett, *J. Mater. Chem.*, 2011, **21**, 7651.
- 15 S. Arora, T. Mathew and N. Batra, *J. Phys. D: Appl. Phys.*, 1990, **23**, 460.
- 16 P. Pandey, N. Bhawe and R. Kharat, *Mater. Lett.*, 2005, **59**, 3149.
- 17 J. Y. Zheng, G. Song, C. W. Kim and Y. S. Kang, *Electrochim. Acta*, 2012, **69**, 340.
- 18 J. Yourey, J. Kurtz and B. Bartlett, *J. Phys. Chem. C*, 2012, **116**, 3200.
- 19 J. Wu, F. Duan, Y. Zheng and Y. Xie, *J. Phys. Chem. C*, 2007, **111**, 12866.
- 20 Y. Huang, Z. Ai, W. Ho, M. Chen and S. Lee, *J. Phys. Chem. C*, 2010, **114**, 6342.
- 21 C. Wang, H. Zhang, F. Li and L. Zhu, *Environ. Sci. Technol.*, 2010, **44**, 6843.
- 22 F. Amano, A. Yamakata, K. Nogami, M. Osawa and B. Ohtani, *J. Phys. Chem. C*, 2011, **115**, 16598.
- 23 A. Kudo and S. Hiji, *Chem. Lett.*, 1999, 1103.
- 24 T. Saison, N. Chemin, C. Chaneac, O. Durupthy, V. Ruaux, L. Mariey, F. Mauge, P. Beaunier and J. Jolivet, *J. Phys. Chem. C*, 2011, **115**, 5657.
- 25 C. Ng, A. Iwase, Y. H. Ng and R. Amal, *J. Phys. Chem. Lett.*, 2012, **3**, 913.
- 26 A. K. P. Mann, E. M. P. Steinmiller and S. E. Skrabalak, *Dalton Trans.*, 2012, **41**, 7939.
- 27 A. Walsh, Y. Yan, M. Huda, M. Al-Jassim and S.-H. Wei, *Chem. Mater.*, 2009, **21**, 547.
- 28 A. Kudo, K. Omori and H. Kato, *J. Am. Chem. Soc.*, 1999, **121**, 11459.
- 29 M. Huda, Y. Yan and M. Al-Jassim, *J. Appl. Phys.*, 2011, **109**, 113710.
- 30 A. Walsh, G. Watson, D. Payne, R. Edgell, J. Guo, P.-A. Glans, T. Learmonth and K. Smith, *Phys. Rev. B: Condens. Matter Mater. Phys.*, 2006, **73**, 235104.
- 31 Y. Liang, T. Tsubota, L. Mooij and R. van de Krol, *J. Phys. Chem. C*, 2011, **115**, 17594.
- 32 H. Dotan, K. Sivula, M. Gratzel, A. Rothschild and S. Warren, *Energy Environ. Sci.*, 2011, **4**, 958.
- 33 K. Itoh and J. O. M. Bockris, *J. Electrochem. Soc.*, 1984, **131**, 1266.
- 34 A. J. Nozik, *Annu. Rev. Phys. Chem.*, 1978, **29**, 189.
- 35 S. R. Morrison, in *Electrochemistry at Semiconductor and Oxidized Metal Electrodes*, Plenum Press, New York, 1980, pp. 49–78.
- 36 M. Walter, E. Warren, J. McKone, S. Boettcher, Q. Mi, E. Santori and N. Lewis, *Chem. Rev.*, 2010, **110**, 6446.
- 37 J. Seabold and K.-S. Choi, *J. Am. Chem. Soc.*, 2012, **134**, 2186.